Local heat dissipation and elasticity of suspended silicon nanowires revealed by dual scanning electron and thermal microscopies

Jose M Sojo-Gordillo, Gerard Gadea-Diez, David Renahy, Marc Salleras, Carolina Duque-Sierra, Pascal Vincent, Luis Fonseca, Pierre-Olivier Chapuis, Alex Morata, Séverine Gomès, et al.

Local heat dissipation and elasticity of suspended silicon nanowires revealed by dual scanning electron and thermal microscopies

Jose M. Sojo-Gordillo,[*,†,‡] Gerard Gadea-Diez,[‡] David Renahy,[¶,§] Marc Salleras,[‖] Carolina Duque-Sierra,[†] Pascal Vincent,[§] Luis Fonseca,[‖] Pierre-Olivier Chapuis,[*,¶] Alex Morata,[*,†] Séverine Gomès,[*,¶] and Albert Tarancón[†,⊥]

†*Catalonia Institute for Energy Research, IREC, Jardins de les Dones de Negre 1, 08930, Sant Adrià de Besòs, Barcelona*

‡*University of Basel, Klingelbergstrasse 82, 4056, Basel, Switzerland*

¶*Université de Lyon, CNRS, INSA-Lyon, Université Claude Bernard Lyon 1, CETHIL UMR5008, F-69621, Villeurbanne, France*

§*Université de Lyon, Université Clade Bernard Lyon 1, CNRS, Institut Lumière Matière, F-69622, Villeurbanne, France*

‖*Institute of Microelectronics of Barcelona, IMB-CNM (CSIC), C/Til·lers s/n, Campus UAB, Bellaterra, 08193, Barcelona, Spain*

⊥*ICREA, Passeig de Lluís Companys, 23, 08010 Barcelona, Spain*

E-mail: jose.sojo@unibas.ch; pierre-olivier.chapuis@insa-lyon.fr; amorata@irec.cat; severine.gomes@insa-lyon.fr

Abstract

A novel combined setup, with a Scanning Thermal Microscope (SThM) embedded in a Scanning Electron Microscope (SEM), is used to characterize a suspended silicon rough nanowire, which is epitaxially clamped at both sides and therefore monolithically integrated in a microfabricated device. The rough nature of the nanowire surface, which prohibits vacuum-SThM due to loose contact for heat dissipation, is circumvented by decorating the wire with periodic platinum dots. Reproducible approaches over these dots, enabled by the live feedback image provided by the SEM, yield a strong improvement in thermal contact resistance and a higher accuracy in its estimation. The results – thermal resistance at the tip-sample contact of $188 \pm 3.7\,\mathrm{K/\mu W}$ and thermal conductivity of the nanowire of $13.7 \pm 1.6\,\mathrm{W/m{\cdot}K}$ – are obtained by performing a series of approach curves on the dots. Noteworthy, the technique allows measuring elastic properties at the same time – the moment of inertia of the nanowire is found to be $(6.1 \pm 1.0) \times 10^{-30}\,\mathrm{m}^4$ –, which permits to correlate the respective effects of the rough shell on heat dissipation and on the nanowire stiffness. The work highlights the capabilities of the dual SThM/SEM instrument, in particular the interest of systematic approach curves with well-positioned and monitored tip motion.

Introduction

Over the last years, nanotechnology has become more and more accessible thanks to the standardization of fabrication processes. Progressively sophisticated nanostructures have become available, such as thin films, nanodots, or nanowires, which have found a wide range of applications in the fields of photonics, quantum computing, or catalysis among others.[1–5] One of the breakthrough possibilities that these materials offer is the high dependence of the thermal conductance with the size. This feature allows fine control of heat transport. This finds a very direct application in thermoelectric materials, where the decoupling of the thermal conductivity from the electronic properties has yielded highly efficient thermoelectric nanomaterials.[6,7]

In order to follow the progress of new micro- and nano-structural concepts, instrumentation and measurement techniques suitable for these scales are in constant development. Numerous techniques are currently available for exploring thermal transport in materials at such scales, with some of the most common ones relying on the assessment of changes in electrical conductivity. These techniques, such as the 3ω method[8] or nanocalorimeters,[9] require the implementation of the materials on complex microdevices, which differ significantly from the actual integration conditions. On the other hand, alternative techniques based on optical variations such as thermoreflectance[10] and micro-Raman thermography[11] offer advantages such as faster measurements, non-invasiveness, and lower complexity in sample preparation. However they are all limited in spatial resolution due to the light diffraction limit. Additionally, accurately determining the absorbed input power, a crucial parameter for determining thermal properties, can be challenging. In this context, Scanning Probe Microscopy (SPM)-based techniques – more specifically Scanning Thermal Microscopy (SThM) – provide a nanometer-scale spatially resolved alternative.[12] Indeed, this technique has been widely applied to 2D nanostructures such as thin films, suspended membranes and even 2D materials such as graphene.[13,14] However, one of the most challenging aspects during the first decades of development of the technique has been the lack of quantitative methods for

the analysis of the sample conductance, due to the complex shape of the sensors and their contacts with the samples. This issue has been partially solved by the development of Finite Element Method (FEM) models of the probes.[15–17]

A limitation of this technique is that most commonly used commercial SThM probes such as the micrometric Wollaston or the nanometric Pd/nitride thin film one present large apex angles ($\sim 45\,^{\circ}$)[18–20] and thus they easily suffer of lateral interaction over high aspect ratio samples.[21] Over these types of samples, the signal change due to variations in the contact area can be of the same order of magnitude as the signal of the nano/microstructure of interest as it will be discussed along this work. Hence, the access to the intrinsic material properties becomes complex in these cases since the noise subtraction is often extremely difficult to perform. In a prior work, some of the authors applied a procedure based on performing discrete z-approaches with the aim of overcoming this issue.[21] However, accurately aiming the aforementioned approaches over the samples remains challenging even if a topography map can be performed without damaging the sample. This issue motivated a first generation of combined SEM/SPM systems.[22–24]

In this context, this works presents the first-time reported use of a dual scanning electron and thermal microscope setup for probing a suspended nanowire. This investigation allows determining simultaneously the mechanical and thermal properties of high aspect ratio nanostructures. Here, a horizontally suspended epitaxially integrated silicon nanowire is studied. A discrete z-approach SThM procedure is used, similar to that developed previously[21] but in vacuum and with live monitoring of the tip position. The thermal study is enabled by solving the issue of uncontrolled tip-sample contact in vacuum. Quantitative analysis of the data is achieved by fine-tuning a Finite Element Method model of the employed Pd/nitride thin film probe. It is shown that while decreasing thermal conductivity the rough shell of the nanowire actually makes it stiffer.

Results and discussion

System and sample description

The NW studied in this work is expitaxially integrated at both ends in the same way as those NWs reported in prior works,[21,25,26] as illustrated in Figure 1a. The NW has a length of 17.3 µm, an average diameter of 57.2 nm, and it is suspended at a distance of 2.5 µm over the substrate (see Figure S1). A rough surface full of protuberances with an average thickness of roughly 50 nm resulting from the growth process of the NW[25] is observed (see Figure S1). Additionally, several platinum dots were selectively deposited along the NW length. These nanodots are expected to increase the tip-NW contact area[27,28] and thus reduce the high thermal contact resistance expected in vacuum[29] and homogenize this value along the NW. Indeed, the roughness of the NW is a challenge for vacuum-operated SThM and, furthermore, it presents a noticeable length dependence. Additionally, dots also serve as position beacons along the NW length and thus help in the localization of the contact points, reducing the spatial uncertainty. A couple of those dots were deposited over the bulk silicon so they could be used as a reference for the thermal contact resistance contribution of the dots themselves.

A custom-made AFM system with Attocube piezo-actuators was used in order to perform the experiments, as illustrated in Figure 1b. This AFM can be inserted within a Nova nanoSEM 450 stage (see Figure S2 for further details),[30] which not only provides the vacuum environment but also allows the user to get live visual feedback of the tip-sample relative position as depicted in Figure 1c and d. Contrary to prior SThM experiments in atmospheric conditions,[21] in this approach no topography map prior to the measurements was needed thanks to the higher spatial accuracy of the SEM imaging feedback. Additionally, SEM allows to precisely align an optical fiber over the probe (Figure 1d). This enables the use of a highly sensitive interferometer for the deflection readout instead of the classical reflected laser-photodiode configuration.

The thermal data acquisition subsystem of the set-up relies on a simple Wheatstone

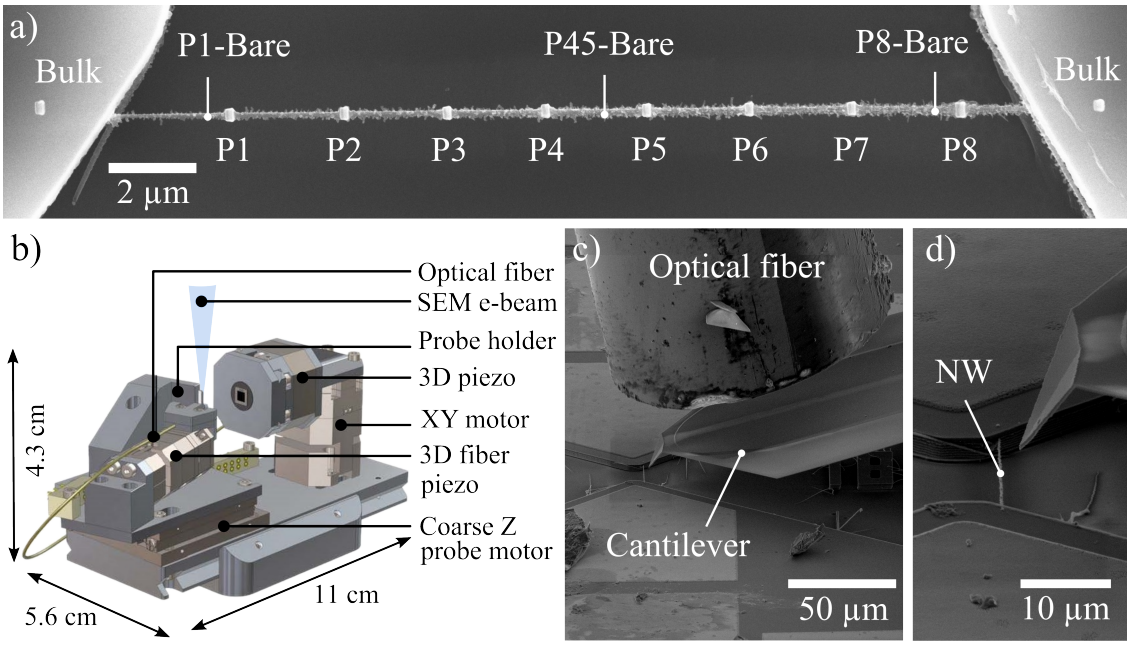

Figure 1: a) SEM top image of the probed NW, showing the Pt dots deposited on the bulk and NW. The position where the probe contacted the bare NW are also indicated. b) Schematics of the AFM set-up. c) Tilted SEM image of the tip close to the sample, showing the cantilever and the optical fiber aligned ∼30 µm above. d) Zoomed view showing the probe apex close to the suspended NW. The convexity of the probe apex over its symmetry plane can be appreciated.

bridge fed by a constant current source (see Figure S3). The system works in temperature contrast mode, where the measured signal (V_{AB}) is amplified by a gain factor K_G, filtered with a low-pass filter with a 3 Hz cut-off frequency, and recorded. The V_{AB} signal is used to obtain the tip electrical resistance R_{tip} by the Wheatstone bridge relationship:

$$R_{tip} = \frac{R_V R_B I_{SP} - V_{AB}/K_G\,(R_A + R_B)}{R_A I_{SP} + V_{AB}/K_G} \tag{1}$$

being I_{SP} the supplied current. Then, using a calibrated factor ($\partial\theta_{tip}/\partial\Delta R_{tip}$), the electrical resistance variations of the tip can be translated into tip temperature variations and related to changes in the overall thermal conductance:

$$G = \frac{\dot{Q}_{tip}}{\theta} = \frac{I_{tip}^2 R_{tip}}{\Delta R_{tip}} \cdot \left(\frac{\partial \Delta R_{tip}}{\partial \theta_{tip}}\right) = \frac{\left(I_{SP}\frac{R_B+R_V}{R_A+R_V+R_B+R_{tip}}\right)^2 R_{tip}}{\Delta R_{tip}} \cdot \left(\frac{\partial \Delta R_{tip}}{\partial \theta_{tip}}\right). \tag{2}$$

A FEM model of the 2$^{\text{nd}}$ generation Pd/nitride probe manufactured by KNT is built upon optical and SEM imaging of the probe (Figure S4). A reduced number of fit parameters is required simultaneously by relating the metal thin film thermal and electrical conductivities through the Wiedemann-Franz law (see Supp. Section: Finite Element Model of the Pd/nitride thin film cantilever). Then, the model is fine-tuned using manufacturer specifications and linear fits of the experimental data. Figure S5 shows the calibration curves, namely an electrical resistance evaluation under different furnace temperatures (Figure S5a) and a self-heating curve under vacuum (Figure S5b). Figure 2a shows the temperature distribution of the SThM probe calculated using the calibrated FEM model. A summary of the parameters used for the model is shown in Table S1. With the FEM model fitted, the tip electrical resistance change while being self-heated can directly be related to changes in the tip apex temperature as shown in the inset of Figure 2b. This slope $\partial\theta_{tip}/\partial\Delta R_{tip}$ value allows using Equation 2 to compute the thermal conductance G changes recorded. Noteworthly, this approach is only valid if the contact with the sample does not alter significantly

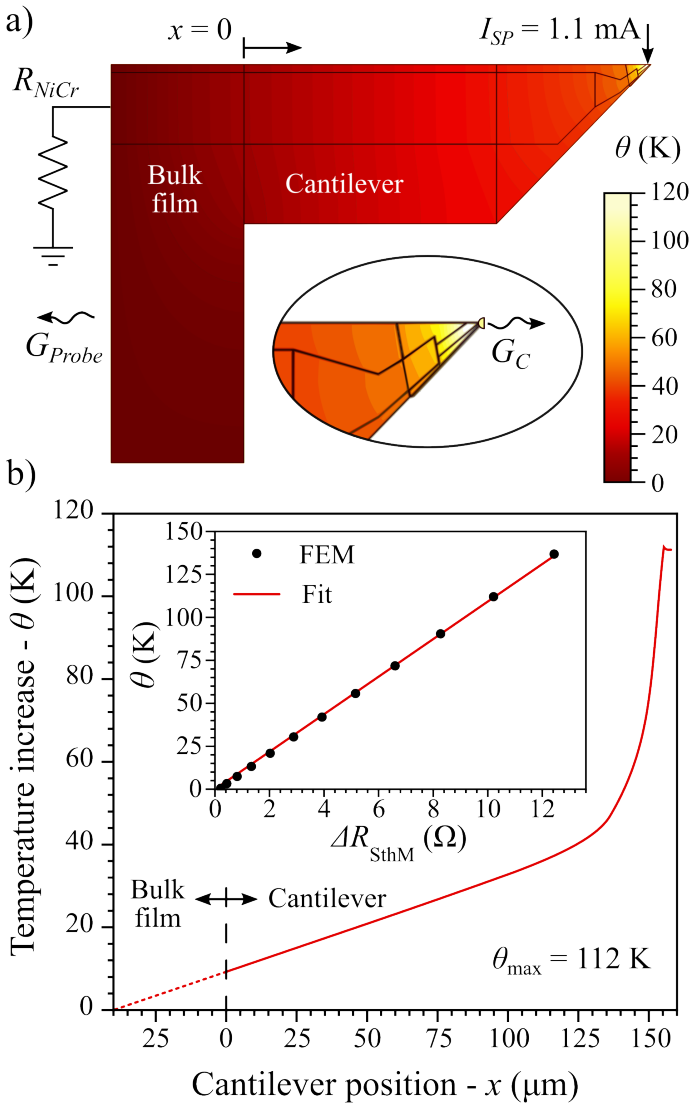

Figure 2: a) FEM solution of the temperature distribution of the calibrated Pd/nitride probe in operation. b) Calculated temperature increase θ as a function of the position along the longitudinal symmetry axis of the probe when $G_C < 20\,\mathrm{nW/K}$. The inset shows the temperature increase at the tip apex as a function of the overall tip resistance variation ΔR.

the temperature distribution on the probe. In other words, if the sample conductance – including the contact – is negligible compared to the cantilever intrinsic conductance. As it shown in Figure S6, this assumption holds for $G_C < 20\,\mathrm{nW/K}$.

Mechanical properties

With the precise positioning of the optical fiber over the SThM tip (see Figure 1d), the interferometer signal can be used to determine the force applied to the NW. The elastic constant of the tip K_{probe} was determined to be $0.155\,\mathrm{N/m}$ after calibration with a reference cantilever as detailed in the experimental Supp. Section: Force calibration.

Figure 3a compares the force curves obtained for approaches over the bulk and different positions along the NW. The slope of the curves after contact or, equivalently, the step of the derivative (Figure 3b), decreases as the position of the tip is more centered on the NW. This slope – or step – represents the equivalent elastic constant of the system K_{eq}. The observed trend is expected for a mechanical system composed of two springs in series (the NW K_{NW} and the probe cantilever K_{probe}) according to the following expression:

$$K_{eq} = \frac{1}{K_{NW}^{-1} + K_{probe}^{-1}}. \tag{3}$$

The NW exhibits a crystalline core and a very rough surface of with branches. In order to study their individual mechanical contributions, the NW is considered as a solid core surrounded by a shell with an effective porosity (inset of Figure 3c). This estimation assumes a fully elastic and in-phase bending of the outer shell, implying a continuous layer behaviour. This is an over-simplification of the mechanics taking place in the rough shell, but it provides straightforward insights about the impact of the shell on the total bending of inertia. Since the NW is epitaxially connected at both ends,[25] the elastic constant as a function of the tip position y can be described using the solution for a double-clamped rod with a punctual force at y (the SThM apex):[31]

$$K_{NW}(y) = \frac{3EIL^3}{(L/2+y)^3\,(L/2-y)^3}, \tag{4}$$

where E is the Young modulus, L the NW length, and I is the NW equivalent bending moment of inertia. The latter accounts for the sum of the solid core with diameter ϕ_{core} (assuming a circular section) and the partially-voided rough shell with thickness $t_{shell} = \phi_{shell}/2 - \phi_{core}/2$ and a solid fraction Ψ. In this simplified model, moments of inertia can be simply added,[32] and the effective one can be described as:

$$I = \frac{\pi}{64}\phi_{core}^4 + \Psi\left(\phi_{shell}^4 - \phi_{core}^4\right). \tag{5}$$

Figure 3c shows the resulting NW elastic constant K_{NW} as a function of the tip position y calculated using Equation 3. Here, K_{eq} values were fitted from the force first derivative as a function of the tip height curves exemplified in Figure 3b using a step function and then averaged for each tip position. The solid line of the chart represents the fit of these data. Since there is no evidence in literature[33–35] that the Young modulus varies for NWs of the studied diameter range, Equation 4 can be used to compute the effective moment of inertia I of the NW. Therefore, a value of $E = 188\,\mathrm{GPa}$ – corresponding to silicon bulk in the <111> direction – can be used.[34,35] In this way, a value for I of $(6.1 \pm 1.0) \times 10^{-30}\,\mathrm{m}^4$ is obtained. This value is significantly larger that the one expected for the silicon NW core alone ($(5.25 \pm 1.0) \times 10^{-31}\,\mathrm{m}^4$) and cannot be explained with lateral displacements in the horizontal plane of the NW, since the SEM feedback proved otherwise. Noteworthy, while the presence of the Pt nanodots could also have a partial role in stiffening the NW, it could not explain it alone, as the coverage fraction of the NW is lower than 10%. Therefore, it is likely that the observed stiffening is the result of the outer shell roughness contributing to the total bending moment of inertia. Using Equation 5 and the dimensions extracted from high-magnification SEM images of Figure S1 (core diameter of 57.2 nm and rough shell of thickness 50 nm) a solid fraction of 15.3 % is calculated. This solid fraction value reasonably

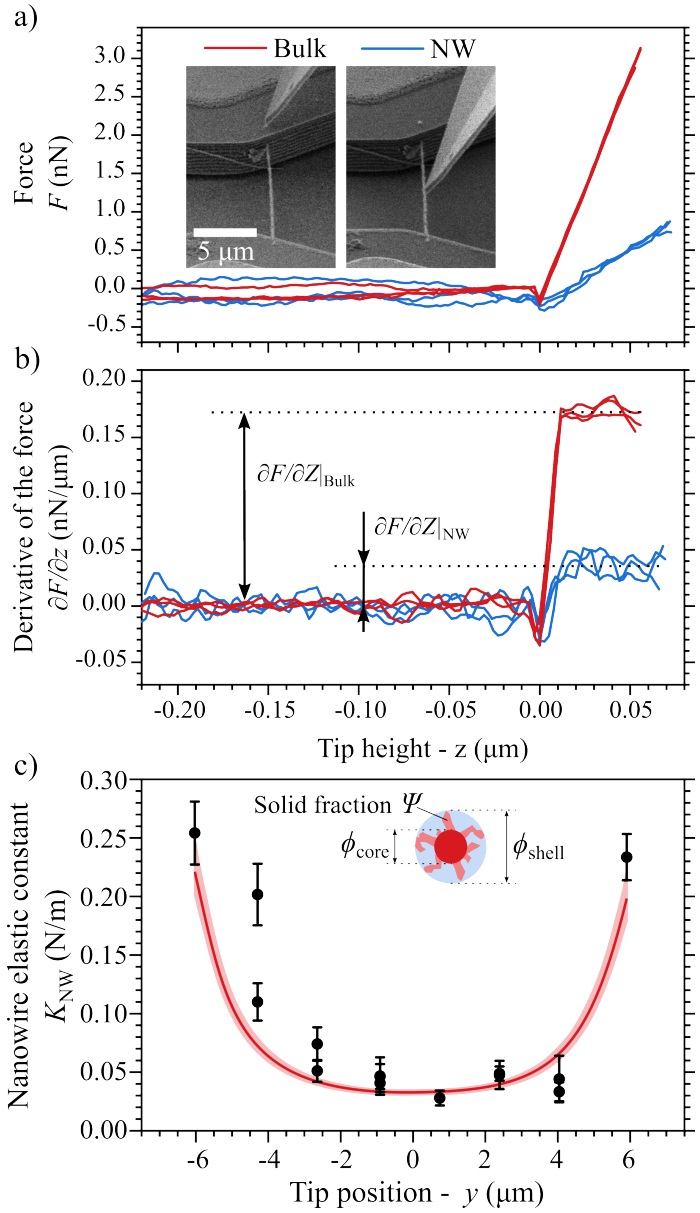

Figure 3: a) Force as a function of tip height curves performed over the bulk (red) and over the central part of the NW (blue). Insets show SEM images of the tip position at the precise moment of contact ($z = 0$). b) First derivative of the force as a function of tip height. Step fits over these curves are used to calculate the equivalent elastic constant K_{eq} at each point. c) Calculated nanowire elastic constant as a function of the tip position along the nanowire from the fitted steps of (b) using Equation 3. Each point is the average of all the approach curves performed over the same point and the error bar represents the stochastic variation. The solid line illustrates the fit of the data using Equation 4. The shadow area represents the systematic error derived from the calibration of the elastic constant scale.

matches the observed morphology of the NW. Hence, while the model used cannot fully catch the details of each of the individual bending contributions of the surface protrusions, this obtained value highlights how the rough shell must play a significant role in the mechanical properties of the NW, acting as a stiffening structure.

Thermal contact resistance

Under vacuum conditions, higher thermal contact resistances are expected since air cannot help in transferring heat across rough or porous zones around the tip-sample mechanical contact, and the contribution of the water meniscus due to ambient humidity is also negligible. Without these two pathways, thermal contact resistances are driven by the solid-solid contact, and become highly dependent on the sample topography and force applied[12,16] among others. Hence, the deposited platinum nanodots illustrated in Figure 1a are expected to homogenize the contact resistances over bulk and NW and to improve heat dissipation towards the core of the nanowire. This strengthens the assumption of using bulk approaches to estimate the probe-dot thermal contact resistance $\Omega_C = 1/G_C$, not likely to be valid over bare nanowires.[21]

Figure 4a shows the thermal conductance change δG – *i.e.* the total conductance G offset by its value prior to the contact – as a function of the piezoelectric displacement in the z axis. These curves were obtained by supplying 1.1 mA through the probe, which corresponds to a tip temperature increase θ_{tip} of 112 K with respect to ambient as shown in Figure 2. Here, θ_{tip} can be considered constant as long as the conductances measured are lower than 20 nW/K as illustrated in Figure S6.

Measurements reported were carried out over the bare silicon surface and over the Pt nanodots deposited on the bulk in order to assess the effects of the latter. From Figure 4a it is not trivial to compute what the true value of G_C is in the bulk case. Alternatively, this can be more easily calculated by plotting the changes in thermal conductances as a function of the force as shown in the right charts of Figure 4. The fitting of the curve after

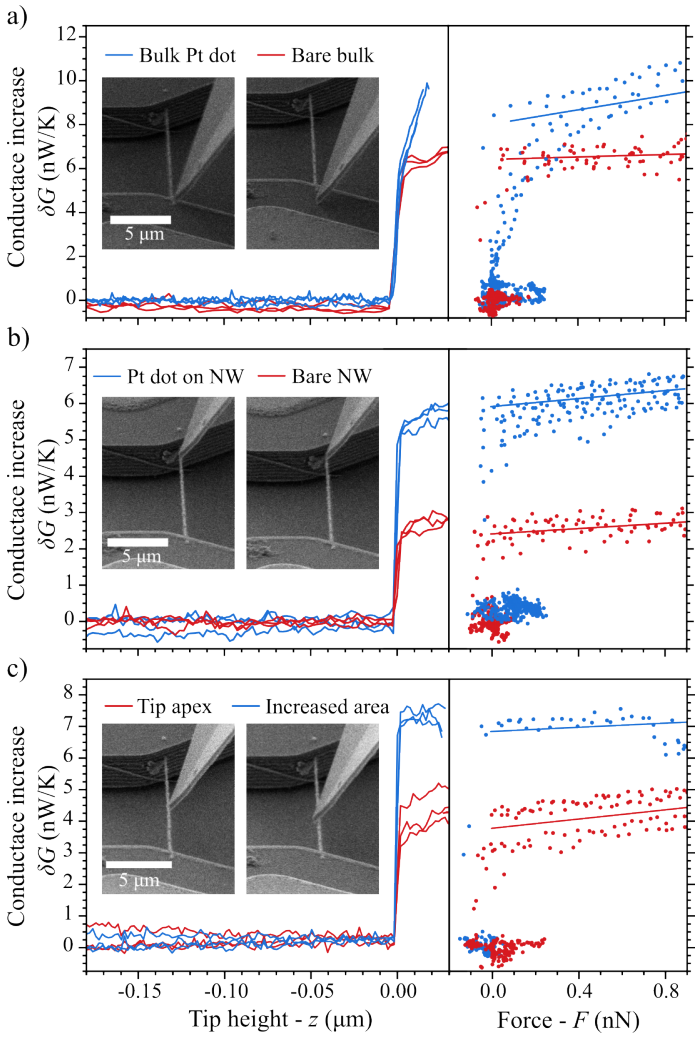

Figure 4: Thermal conductance as a function of the z axis piezoelectric displacement for approaches on different positions of the sample. Insets show SEM images of the tip position at the precise instant of contact ($z = 0$). The right chart shows exact same approach curves (same y scale) plotted as a function of the calculated applied force. A linear fit is performed after the contact. a) Approaches over the bare silicon bulk compared to those over the Pt nanodot. b) Approaches over a bare section of the NW compared to those performed over a Pt nanodot deposited over the NW. c) Approaches over a Pt nanodot on the middle part of the NW. The red approaches correspond to a contact with the tip apex while the blue ones correspond to those with an increased area (moved 100 nm perpendicular to the NW axis).

contact allows determining the true thermal contact conductance as $G_C = G(F = 0)$ and thus $\Omega_C = G_C^{-1}$. Using these curves, Ω_C values of $150 \pm 6.3\,\mathrm{K/\mu W}$ and $188 \pm 3.7\,\mathrm{K/\mu W}$ were evaluated for the contact over Pt nanodots and bare silicon respectively. Calculated values are significantly larger than those reported in other experiments using such tips but taking place at larger pressures (see Table 1). The vacuum conditions achieved here are likely to be responsible for the comparatively-larger Ω_C observed,[36] and closer to those performed under vacuum conditions.[17,27,37,38] Noteworthy, a new version of the commonly used Pd/nitride probes was used in this work. This probe features a convex angle across the symmetry line on the tilted section of the tip and a smaller apex angle respect to the previous models (see Figure 1). This geometry is expected to reduce the contact area and thus G_C with respect to the standard Pd/nitride probes. Additionally, significant changes in the variation of G with the applied force F can be appreciated between both studied cases. A larger dependence when probing the sample over the Pt nanodots ($1.63\,\mathrm{W/K{\cdot}N}$) is observed compared to the contact over bare silicon ($0.27\,\mathrm{W/K{\cdot}N}$). This is likely caused by the indentation of the SThM tip on the Pt nanoparticle, which is softer than the Si bulk.

Table 1: Comparison of different thermal contact resistances for the Pd/Nitride film probe found in literature with the measured values of this work.

Ω_C	T_{Probe}	Sample surface	Pressure	Ref.
(K/µW)	(K)		(mBar)	
4.09 ± 0.11	-	Si^N	1000	[39]
1.15 ± 0.06	421	Au	1000	[40]
4.8 ± 0.31	328	Si ^{N}	1000	[21]
12.5 ± 0.61	376	$Si_{1-x}Ge_x$ ^{N}		
2.3 ± 0.4	338	Si	0.28	[29]
1.4 ± 0.1		Ge		
66.6 ± 4.4	388	Si ^{N}	0.28	[27]
100 ± 40		Si ^{N,R}		
68.9 ± 5.6	-	ZnFeO	1.3×10^{-3}	[17]
41.6 ± 3.5	-	SiO_2	$< 10^{-4}$	[38]
188 ± 3.7	385	Si ^{R,N}	$< 10^{-4}$	This work
150 ± 6.3		Pt		
9.4 ± 0.2	333	Si	10^{-5}	[16]
6.0 ± 0.2	373	Au		
54.5 ± 1	308	SiO_2	2×10^{-6}	[37]

^{N} With a native oxide layer. ^{R} Rough surface.

In Figure 4b, a similar approach is followed over the NW in order to asses the effects of the deposited nanodots compared to the rough surface of the NW. A nanodot close to the bulk is used (P1 of Figure 1a corresponding to a distance from the bulk of 1.4 µm) since the equivalent NW conductance is higher there and thus the differences in G are more evident. As illustrated in the left chart of Figure 4b, a difference of 3.5 K/nW is observed between the contact of both cases. Finally, in this case, the differences in slope are less evident – 0.54 W/K·N for the nanodot case versus the 0.36 W/K·N of the bare NW case – since the NW bending partially masks the indentation effect observed over bulk.

Aside of the effects of the Pt dots on the thermal contact mentioned before, one of the most challenging issues to tackle when probing NWs with SThM is to ensure a reproducible effective contact area along the experiment. As depicted in Figure 4c, the effects of contacting the NW with a part of the tip belly instead of the apex significantly increases the available contact area and thus decreases Ω_C. Here, the NW was first contacted with the probe apex and then it was moved forward – *i.e.* perpendicular to the NW axis – by 100 nm. From Figure 4c, the increase in contact conductance is 3.1 nW/K. The associated reduction in thermal contact resistance can be estimated with the following expression:

$$\Delta\Omega_C^{IA} = \frac{1}{\delta G_{IA}} - \frac{1}{\delta G_{Apex}}. \tag{6}$$

Thus, an increase of 2.7 K/nW – *i.e.* 42% – with respect to the apex value Ω_C^{Apex} is obtained. This result highlights the relevance of a precise tip positioning over the sample in order to ensure consistency among measurements.

Thermal conductivity determination

Figure 5a shows several approach curves on Pt nanodots at different positions along the nanowire axis. A clear evolution can be observed in δG as the tip moved closer to the bulk. Step sizes ranging from 3 nW/K close to the NW center (P3 of Figure 1a) to 7.5 nW/K at

the bulk were observed. In contrast, G_C at the bulk reached up to 7.5 nW/K. Additionally, contact points at the nanowire surface did not show significant differences in the fitted conductance dependence with the applied force shown in the right side of Figure 5a.

The average variation of δG – exemplified in the right side of Figure 5a – corresponds to the contact conductance $G_C = \delta G$, and is provided as a function of the tip position y along the whole NW in Figure 5b. Remarkably, no clear trend could be observed on the set of points measured over the bare nanowire (grey points in Figure 5b), with all of them showing lower G_C than those performed over Pt dots. This indicates that the signal measured is dominated by the contact resistance in such conditions.

Assuming that $G_C(y)$ can be fully attributed to the creation of the new heat dissipation pathway though the NW, the local thermal resistances of the nanowire $\Omega_{NW}(y)$ were calculated using the following expression:[21]

$$\delta G(y)^{-1} = \Omega_C + \Omega_{NW}(y) = \Omega_C + \left(\frac{L}{A\kappa} \left[\frac{1}{4} - \left(\frac{y}{L} \right)^2 \right] \right), \tag{7}$$

where A is the NW cross section, L is the NW length, and Ω_C is the tip-nanodot thermal contact resistance. Using Equation 7 and the Ω_C values estimated before, the longitudinal profile of $\Omega_{NW}(y)$ was resolved and represented in Figure 5c (see Figure S7 to compare with the data acquired over the bare surface of the NWs). The inverse parabolic shape of $\Omega_{NW}(y)$ matches the expected behavior for the double-clamped NW system. The solid line represents the fit of the data using the definition of $\Omega_{NW}(y)$. A fairly good symmetry is observed in the curve and no Ω offset was required for the fit. This is an indication of a very limited – if any – thermal contact resistance between nanowire and bulk – *i.e.* a full epitaxial connection at both ends – that confirms the results of prior works.[25] As result of the fit, a thermal conductivity of 13.7 ±1.6 W/m·K is estimated for the NW. This value agrees with the results obtained using atmospheric SThM of our prior work,[21] but is substantially more accurate in what regards reproducibility of the signal as the stochastic errors alone would yield an uncertainty of ±0.8 W/m·K. It is worth noticing how the accuracy of the

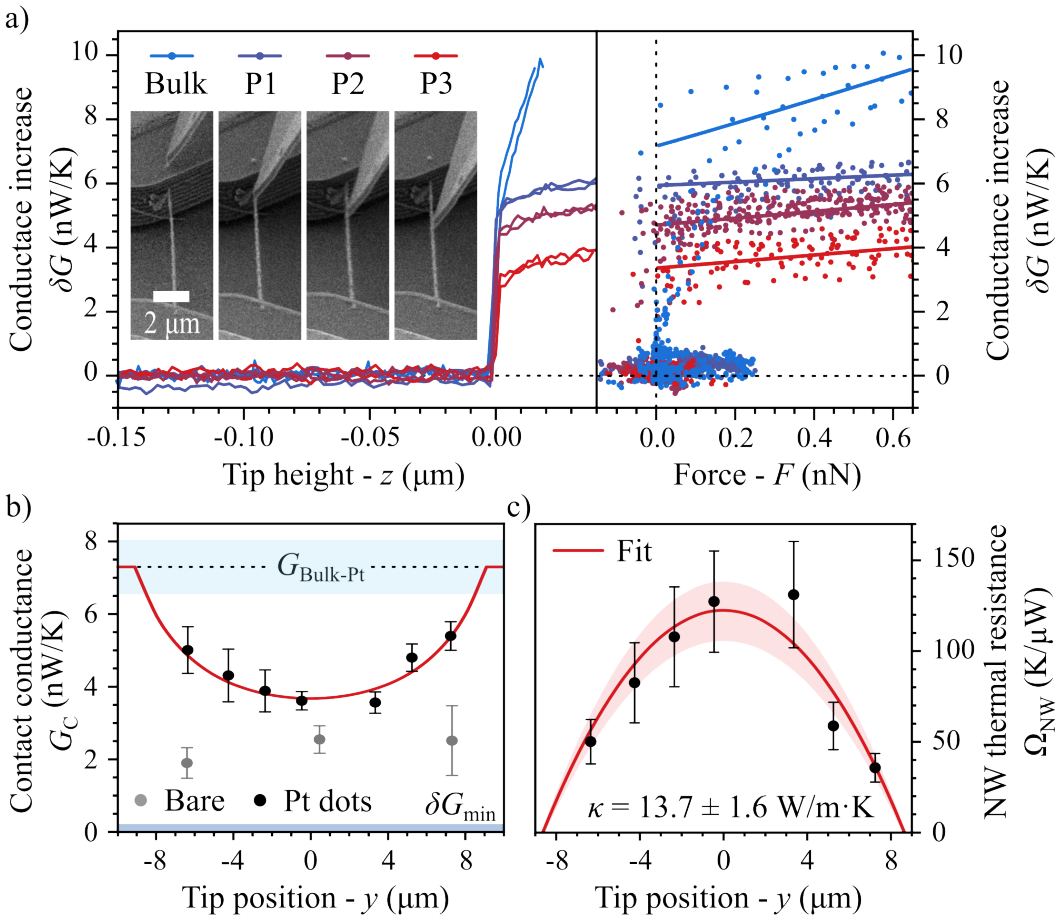

Figure 5: a) Thermal conductance increase as a function of the z axis piezo displacement curves for approaches over different deposited Pt nanodots along the nanowire (left). Insets show SEM images of the tip position at the precise instant of contact ($z = 0$). The right chart shows the thermal conductance increase of the same curves as a function of the force applied. Solid lines represent the linear fit for each curve for all points with $F > 0$. b) Contact conductance G_C as a function of the tip position over the bare NW (grey) and Pt dots (black). Each point is the average of all the approach curves performed over the same point and the error bar represents the stochastic uncertainty. Top shaded area represents the thermal contact conductance expected for Pt dots over the bulk. Bottom shaded area represents the minimum step that could be measured. c) Nanowire local thermal resistance as a function of the tip position. The solid red line represents the fit of the data using Equation 7, while the shadow area represents the systematic error derived from the calibration of the Ω_{NW} scale.

measurement is not limited by the reproducibility of the approaches (stochastic variations), but by the accuracy of the calibration (see Supp. Section: Thermal uncertainty analysis for further details on the uncertainty estimation). The result is consistent with studies relating the degree of surface roughness with an enhanced phonon scattering.[41,42] The value also matches κ estimations performed using fully electrical measurements[26] in the same kind of wires and is also consistent with the theoretical predictions for rough NWs[43–45] employing again a fully diffuse model (specularity parameter $p = 0$) and estimated Surface-to-Volume Ratios (SVR) in the order of $0.015\,\mathrm{nm}^{-1}$.

Conclusions

This work reports the first-time use of a dual SEM-SThM approach for the simultaneous evaluation of thermal and elastic properties of nanowires. It illustrates the advantages of the experiment compared to standard SThM measurements with Pd/nitride probes. A discrete series of z-approaches was carried out in order to probe the studied silicon NW, with recorded curves showing high reproducibility. Combined with an FEM modeling of the SThM probe, this allows obtaining an accurate thermal resistance profile along the studied NW. Mechanical properties of the NW were evaluated at the same time, highlighting the elastic behavior of a double-clamped rod. Noteworthy, the rough surface of the NWs – which can be seen as a porous shell – effectively stiffens the NW. The thermal studies in vacuum were realized by the deposition of Pt nanodots, which reduce and homogenize the tip-sample thermal contact resistance, which is usually uncontrolled for rough structures. The thermal conductivity of the studied nanowire was calculated to be $13.7 \pm 1.6\,\mathrm{W/m{\cdot}K}$, while thermal contact resistance at the clamping of the nanowire could not be singled out, demonstrating the high epitaxial contact. Improvements in the modeling of Pd/nitride thin film SThM probes should foster accuracy, as it is currently the main source of uncertainty.

Overall, the thermal conductance measurements have shown to be a convenient proce-

dure for the thermal evaluation of high aspect ratio integrated nanostructures. The combined SEM/SThM platform offers a very promising instrument for the thermal evaluation of complex integrated nanostructures, in particular electrically-insulating or optically-transparent ones which cannot be addressed by electro-thermal or optical techniques, respectively.

Experimental

Sample preparation

Bottom-up Si NW was grown by means of the Vapour Liquid Solid (VLS) mechanism within a First Nano EasyTube 3000 Chemical Vapour Deposition (CVD) reactor following the procedure described elsewhere.[26,46] The nanodots were deposited using the precursor gas injection system of a Zeiss Auriga SEM. Microdevices were fabricated in cleanroom facilities employing a series of photolithography, metal evaporation and wet and dry etching microfabrication steps.[21,25]

Force calibration

The elastic calibration process of the KNT cantilever consists of the comparison of the tip in-contact deflection sensitivity $\partial z/\partial I_S$ when probed over the bulk and over a reference cantilever of the same material and known elastic constant K_{ref}. Thus, the following expression can be used:[47,48]

$$K = K_{ref}\left(\frac{\partial z/\partial I_S|_{ref}}{\partial z/\partial I_S|_{bulk}} - 1\right)\left(\frac{L}{L-\Delta L}\right)^3 \tag{8}$$

where L is the reference cantilever length, ΔL is the distance from the edge of the reference cantilever to the contact point and I_S is the photodiode/interferometer signal.

Thermal calibration

The thermal calibration process of the Pd/nitride thin film probe is detailed in the following steps: i) A self-heating curve is carried out in vacuum, as represented in Figure S5a. This curve is also used to identify a supplied current value that does not generate self-heating. ii) Overall tip electrical resistance direct evaluation under homogeneous furnace temperatures is carried out. Supplied current is set to a low value, preventing self-heating effects. iii) A probe FEM model is built according to the probe manufacturer specifications and refined using optical and SEM images of the tip Figure S4, allowing to determine shapes with sub-micrometer uncertainties. A key part of the process is to obtain self-consistent values for the electrical resistances and temperature coefficient of electrical resistances for the different materials involved (see Supp. Section: Finite Element Model of the Pd/nitride thin film cantilever for explanations). Note that the FEM step is required due to the complex shape of the probe and the fact that homogeneous heating and self-heating cannot be matched without including such a feature. The model is adjusted using the experimental data acquired in the first two points. iv) The customized FEM model is used to predict the temperature at the tip apex as a function of the resistance of that particular tested probe. This calibration curve allows converting the measured electrical resistance variations in changes of temperature, which can be subsequently translated into thermal conductances using Equation 2.

Acknowledgement

This investigation has been supported by the Spanish Ministry of Education through the FPU grant **FPU18/01494**, and by the University and Research Secretary of the Business and Knowledge Department of the Generalitat de Catalonia in the project *FEM-IoT* (**001-P-001662**). This research as also been supported by the Spanish National Research Agency (AEi) though the project **PID2019-110142RB-C21** (AEI/FEDER, EU) *THERMOLOGICS*. This research has used the Spanish ICTS Network *MICRONANOFABS*, par-

tially funded by FEDER funds through *MINATEC-PLUS-2* project **FICTS2019-02-40**. This work has also been supported by the French National Research Agency (ANR) through the projects *TIPTOP* **ANR-16-CE09-0023** and the project *ATTSEM* **ANR-10-LABX-0064** (LabEx iMUST). The European Commission also supported this investigation through the *EFINED* project **H2020-FETOPEN-2016-2017** (GA 766853) and the *QUANTIHEAT* project **NMP-2013-LARGE-7** (GA 604668).

Supporting Information Available

Additional referenced figures and tables as well as details of the calibration process are provided in the Supplementary Information. Raw data employed in the elaboration of this work can be found online in the repository Dataset for *Local heat dissipation and elasticity of suspended silicon nanowires revealed by dual scanning electron and thermal microscopies*.

References

(1) Holm, J. V.; Jørgensen, H. I.; Krogstrup, P.; Nygård, J.; Liu, H.; Aagesen, M. Surface-passivated GaAsP single-nanowire solar cells exceeding 10% efficiency grown on silicon. *Nature Communications* **2013**, *4*.

(2) Versteegh, M. A.; Reimer, M. E.; Jöns, K. D.; Dalacu, D.; Poole, P. J.; Gulinatti, A.; Giudice, A.; Zwiller, V. Observation of strongly entangled photon pairs from a nanowire quantum dot. *Nature Communications* **2014**, *5*.

(3) Pan, C.; Dong, L.; Zhu, G.; Niu, S.; Yu, R.; Yang, Q.; Liu, Y.; Wang, Z. L. High-resolution electroluminescent imaging of pressure distribution using a piezoelectric nanowire LED array. *Nature Photonics* **2013**, *7*, 752–758.

(4) Tomioka, K.; Yoshimura, M.; Fukui, T. A III-V nanowire channel on silicon for high-performance vertical transistors. *Nature* **2012**, *488*, 189–192.

(5) Pacios Pujadó, M.; Sojo Gordillo, J. M.; Avireddy, H.; Cabot, A.; Morata, A.; Tarancón, A. Highly Sensitive Self-Powered H_2 Sensor Based on Nanostructured Thermoelectric Silicon Fabrics. *Advanced Materials Technologies* **2020**, *2000870*, 2000870.

(6) Noyan, I. D.; Gadea, G.; Salleras, M.; Pacios, M.; Calaza, C.; Stranz, A.; Dolcet, M.; Morata, A.; Tarancon, A.; Fonseca, L. SiGe nanowire arrays based thermoelectric microgenerator. *Nano Energy* **2019**, *57*, 492–499.

(7) Estrada-Wiese, D.; Sojo, J.-M.; Salleras, M.; Santander, J.; Fernandez-Regulez, M.; Martin-Fernandez, I.; Morata, A.; Fonseca, L.; Tarancon, A. Harvesting performance of a planar thermoelectric microgenerator with a compact design. 2021 IEEE 20th International Conference on Micro and Nanotechnology for Power Generation and Energy Conversion Applications (PowerMEMS). 2021; pp 108–111.

(8) Lu, L.; Yi, W.; Zhang, D. L. 3–ω method for specific heat and thermal conductivity measurements. *Review of Scientific Instruments* **2001**, *72*, 2996–3003.

(9) Li, D.; Wu, Y.; Kim, P.; Shi, L.; Yang, P.; Majumdar, A. Thermal conductivity of individual silicon nanowires. *Applied Physics Letters* **2003**, *83*, 2934–2936.

(10) Regner, K. T.; Sellan, D. P.; Su, Z.; Amon, C. H.; McGaughey, A. J.; Malen, J. A. Broadband phonon mean free path contributions to thermal conductivity measured using frequency domain thermoreflectance. *Nature Communications* **2013**, *4*.

(11) Doerk, G. S.; Carraro, C.; Maboudian, R. Single Nanowire Thermal Conductivity Measurements by Raman Thermography. *ACS Nano* **2010**, *4*, 4908–4914.

(12) Gomès, S.; Assy, A.; P. Olivier, C. Scanning thermal microscopy: A review. *Phys. Status Solidi A* **2015**, *212*, 477–494.

(13) Nguyen, T. P.; Lemaire, E.; Euphrasie, S.; Thiery, L.; Teyssieux, D.; Briand, D.; Vairac, P. Microfabricated high temperature sensing platform dedicated to scanning thermal microscopy (SThM). *Sensors and Actuators: A. Physical* **2018**,

(14) El Sachat, A.; Köenemann, F.; Menges, F.; Del Corro, E.; Garrido, J. A.; Sotomayor Torres, C. M.; Alzina, F.; Gotsmann, B. Crossover from ballistic to diffusive thermal transport in suspended graphene membranes. *2D Materials* **2019**, *6*, 025034.

(15) Spiece, J.; Evangeli, C.; Lulla, K.; Robson, A.; Robinson, B.; Kolosov, O. Improving accuracy of nanothermal measurements via spatially distributed scanning thermal microscope probes. *Journal of Applied Physics* **2018**, *124*, 015101.

(16) Pernot, G.; Metjari, A.; Chaynes, H.; Weber, M.; Isaiev, M.; Lacroix, D. Frequency domain analysis of 3ω-scanning thermal microscope probe-Application to tip/surface thermal interface measurements in vacuum environment. *Journal of Applied Physics* **2021**, *129*.

(17) Alikin, D.; Zakharchuk, K.; Xie, W.; Romanyuk, K.; Pereira J., M.; Arias-Serrano, B. I.; Weidenkaff, A.; Kholkin, A.; V. Kovalevsky, A.; ; Tselev, A. Quantitative Characterization of Local Thermal Properties in Thermoelectric Ceramics Using "Jumping-Mode" Scanning Thermal Microscopy. *Small methods* **2023**, *7*, 14.

(18) Massoud, A. M.; Bluet, J. M.; Lacatena, V.; Haras, M.; Robillard, J. F.; Chapuis, P. O. Native-oxide limited cross-plane thermal transport in suspended silicon membranes revealed by scanning thermal microscopy. *Applied Physics Letters* **2017**, *111*.

(19) Lefèvre, S.; Volz, S.; Saulnier, J. B.; Fuentes, C.; Trannoy, N. Thermal conductivity calibration for hot wire based dc scanning thermal microscopy. *Review of Scientific Instruments* **2003**, *74*, 2418–2423.

(20) Etienne Puyoo, Caractérisation thermique de nanofils de silicium pour des applications à la thermoélectricité. Ph.D. thesis, University of Bordeaux, 2010.

(21) Sojo Gordillo, J. M.; Gadea Diez, G.; Pacios Pujadó, M.; Salleras, M.; Estrada-Wiese, D.; Dolcet, M.; Fonseca, L.; Morata, A.; Tarancón, A. Thermal conductivity of individual Si and SiGe epitaxially integrated NWs by scanning thermal microscopy. *Nanoscale* **2021**, *13*, 7252–7265.

(22) Renahy, D.; Assy, A.; Gomès, S. A Combined SThM/SEM Instrument For The Investigation Of Influent Parameters In Nano-scale Thermal Contact. International Workshop on Thermal Investigations of ICs and Systems. Paris, France, 2015.

(23) Gomès, S.; Renahy, D.; Vincent, P. A Combined SThM/SEM Instrument For The Investigation Of Influent Parameters In Nano-scale Thermal Contact. Minicolloque Nanoconduction et Nanoradiation, Journées de la Matière Condensée. Bordeaux, France, 2016.

(24) Altes, A.; Joachimsthaler, I.; Zimmermann, G.; Heiderhoff, R.; Balk, L. SEM/SThM-hybrid-system: a new tool for advanced thermal analysis of electronic devices. Proceedings of the 9th International Symposium on the Physical and Failure Analysis of Integrated Circuits (Cat. No.02TH8614). 2002; pp 196–200.

(25) Gadea Díez, G.; Sojo Gordillo, J. M.; Pacios Pujadó, M.; Salleras, M.; Fonseca, L.; Morata, A.; Tarancón Rubio, A. Enhanced thermoelectric figure of merit of individual Si nanowires with ultralow contact resistances. *Nano Energy* **2020**, *67*, 104191.

(26) Sojo-Gordillo, J. M.; Estrada-Wiese, D.; Duque-Sierra, C.; Gadea Diez, G.; Salleras, M.; Fonseca, L.; Morata, A.; Tarancón, A. Tuning the thermoelectric properties of boron-doped silicon nanowires integrated into a micro-harvester. *Advanced Materials Technologies* **2022**, *7*.

(27) Guen, E.; Chapuis, P.-O.; Kaur, N. J.; Klapetek, P.; Gomés, S. Impact of roughness on heat conduction involving nanocontacts. *Applied Physics Letters* **2021**, *119*, 161602.

(28) Swami, R.; Julie, G.; Singhal, D.; Paterson, J.; Maire, J.; Le-Denmat, S.; Motte, J.; Gomes, S.; Bourgeois, O. Electron beam lithography on non-planar, suspended, 3D AFM cantilever for nanoscale thermal probing. *Nano Futures* **2022**, *6*, 025005.

(29) Assy, A.; Gomès, S. Heat transfer at nanoscale contacts investigated with scanning thermal microscopy. *Applied Physics Letters* **2015**, *107*, 043105.

(30) Gomès, S.; Renahy, D.; Assy, A.; Vincent, P. Dual Electron and Thermal Scanning Microscopies for advanced nanoscale heat transport analysis. *Small Methods (submitted)* **2023**,

(31) Paulo, A. S.; Bokor, J.; Howe, R. T.; He, R.; Yang, P.; Gao, D.; Carraro, C.; Maboudian, R. Mechanical elasticity of single and double clamped silicon nanobeams fabricated by the vapor-liquid-solid method. *Applied Physics Letters* **2005**, *87*, 1–4.

(32) Cleland, A. N. *Foundations of Nanomechanics*; Springer, 2003.

(33) Sohn, Y. S.; Park, J.; Yoon, G.; Song, J.; Jee, S. W.; Lee, J. H.; Na, S.; Kwon, T.; Eom, K. Mechanical Properties of Silicon Nanowires. *Nanoscale Research Letters* **2010**, *5*, 211–216.

(34) Zhu, Y.; Xu, F.; Qin, G.; Fung, W. Y.; Lu, W. Mechanical properties of Vapor–Liquid–Solid synthesized silicon nanowires. *Nano Letters* **2009**, *9*, 3934–3939.

(35) Gordon, M. J.; Baron, T.; Dhalluin, F.; Gentile, P.; Ferret, P. Size Effects in Mechanical Deformation and Fracture of Cantilevered Silicon Nanowires. *Nano Letters* **2009**, *9*, 525–529.

(36) Assy, A.; Lefèvre, S.; Chapuis, P. O.; Gomès, S. Analysis of heat transfer in the water meniscus at the tip-sample contact in scanning thermal microscopy. *Journal of Physics D: Applied Physics* **2014**, *47*, 1–5.

(37) Gonzalez-Munoz, S.; Agarwal, K.; Castanon, E. G.; Kudrynskyi, Z. R.; Kovalyuk, Z. D.; Spièce, J.; Kazakova, O.; Patanè, A.; Kolosov, O. V. Direct Measurements of Anisotropic Thermal Transport in γ-InSe Nanolayers via Cross-Sectional Scanning Thermal Microscopy. *Advanced Materials Interfaces* **2023**, *10*, 2300081.

(38) Umatova, Z.; Zhang, Y.; Rajkumar, R.; Dobson, P. S.; Weaver, J. M. R. Quantification of atomic force microscopy tip and sample thermal contact. *Review of Scientific Instruments* **2019**, *90*, 095003.

(39) Puyoo, E.; Grauby, S.; Rampnoux, J.-M.; Rouvière, E.; Dilhaire, S. Scanning thermal microscopy of individual silicon nanowires. *Journal of Applied Physics* **2011**, *109*, 024302.

(40) Reihani, A.; Yan, S.; Luan, Y.; Mittapally, R.; Meyhofer, E.; Reddy, P. Quantifying the temperature of heated microdevices using scanning thermal probes. *Applied Physics Letters* **2021**, *118*, 163102.

(41) Lim, J.; Hippalgaonkar, K.; Andrews, S. C.; Majumdar, A.; Yang, P. Quantifying surface roughness effects on phonon transport in silicon nanowires. *Nano Lett* **2012**, *12*, 2475–2482.

(42) Maurer, L. N.; Aksamija, Z.; Ramayya, E. B.; Davoody, A. H.; Knezevic, I. Universal features of phonon transport in nanowires with correlated surface roughness. *Applied Physics Letters* **2015**, *106*, 133108.

(43) Wang, Z.; Mingo, N. Diameter dependence of SiGe nanowire thermal conductivity. *Applied Physics Letters* **2010**, *97*, 101903.

(44) Ohishi, Y.; Xie, J.; Miyazaki, Y.; Aikebaier, Y.; Muta, H.; Kurosaki, K.; Yamanaka, S.; Uchida, N.; Tada, T. Thermoelectric properties of heavily boron- and phosphorus-doped silicon. *Japanese Journal of Applied Physics* **2015**, *54*, 071301.

(45) Yang, H.-Y.; Chen, Y.-L.; Zhou, W.-X.; Xie, G.-F.; Xu, N. Ultra-low thermal conductivity of roughened silicon nanowires: Role of phonon-surface bond order imperfection scattering. *Chinese Physics B* **2020**, 0–14.

(46) Noyan, I. D.; Dolcet, M.; Salleras, M.; Stranz, A.; Calaza, C.; Gadea, G.; Pujadó, M. P.; Álex Morata,; Tarancón, A.; Fonseca, L. All-silicon thermoelectric micro/nanogenerator including a heat exchanger for harvesting applications. *Journal of Power Sources* **2019**, *413*, 125–133.

(47) Hutter, J. L.; Bechhoefer, J. Calibration of atomic-force microscope tips. *Review of Scientific Instruments* **1993**, *64*, 1868–1873.

(48) Ohler, B. Cantilever spring constant calibration using laser Doppler vibrometry. *Review of Scientific Instruments* **2007**, *78*, 063701.

(49) Pic, A. Numerical and experimental investigations of self-heating phenomena in 3D Hybrid Bonding imaging technologies. Ph.D. thesis, INSA-Lyon, 2019.

(50) Guen, E. Microscopie thermique à sonde locale: étalonnages, protocoles de mesure et applications quantitatives sur des matériaux nanostructurés. Ph.D. thesis, INSA-Lyon, 2020.

(51) Assy, A. Development of two techniques for thermal characterization of materials : Scanning Thermal Microscopy (SThM) and 2ω method. Ph.D. thesis, Centre d'Energétique et de Thermique de Lyon, 2015.

(52) Wedler, G.; Alshorachi, G. The influence of thickness on the resistivity, the temperature coefficient of resistivity and the thermoelectric power of evaporated palladium films at 77 K and 273 K. *Thin Solid Films* **1980**, *74*, 1–16.

(53) Vinayak, S.; Vyas, H.; Muraleedharan, K.; Vankar, V. Ni-Cr thin film resistor fabrication for GaAs monolithic microwave integrated circuits. *Thin Solid Films* **2006**, *514*, 52–57.

(54) Ftouni, H.; Blanc, C.; Tainoff, D.; Fefferman, A. D.; Defoort, M.; Lulla, K. J.; Richard, J.; Collin, E.; Bourgeois, O. Thermal conductivity of silicon nitride membranes is not sensitive to stress. *Physical Review B - Condensed Matter and Materials Physics* **2015**, *92*.

(55) Pic, A.; Gallois-Garreignot, S.; Fiori, V.; Chapuis, P.-O. Microelectronics thin films and boundaries characterized by local electro-thermal measurements. 23rd International Workshop on Thermal Investigations of ICs and Systems (THERMINIC). Amsterdam, 2017; pp 1–6, ISSN: 2474-1523.

(56) Zhang, Y.; Zhu, W.; Hui, F.; Lanza, M.; Borca-Tasciuc, T.; Rojo, M. M. A Review on Principles and Applications of Scanning Thermal Microscopy (SThM). *Advanced Functional Materials* **2020**, *30*, 1900892.

Local heat dissipation and elasticity of suspended silicon nanowires revealed by dual scanning electron and thermal microscopies – Supplementary Information

Finite Element Model of the Pd/nitride thin film cantilever

The conversion of measured tip resistance change in thermal conductances described by Equation 2 of the core manuscript relies on the use of a Finite Element Model (FEM) of the tip as highlighted in Figure 2a. Geometrical dimensions were determined from the probe analysis performed in Figure S4 and fixed constants. As depicted in the right lower corner of Figure 1c, because the bulk material was over-etched at the base of the nitride cantilever in the used tip, a fraction of the membrane needs to be simulated as well in order to account for this additional thermal resistance. The only geometrical free parameters were the gold and platinum thicknesses which were used to adjust each of the tip electrical resistances, namely Pd, Au, and NiCr thin films. In order to avoid many computationally expensive simulations with the FEM code, a first approximation of those values could be carried out using the approaches described by Puyoo *et al.*,[20] Pic *et al.*[49] and Guen *et al.*[50] It consists in solving the following system of equations:

$$R_{tip} = R_{Pd} + R_{Au} + R_{NiCr} \tag{S1}$$

$$R_{tip}\,\alpha_{tip} = R_{Pd}\,\alpha_{Pd} + R_{Au}\,\alpha_{Au} + R_{NiCr}\,\alpha_{NiCr}, \tag{S2}$$

where the tip global electrical resistance R_{tip} and its temperature coefficient of resistance α_{tip} can be determined from the data of Figure S5a. Complementary, as described in Table S1, R_{NiCr} was directly measured using microprobes, and the different material temperature coefficients of resistance α_i are taken from the literature.[20,51] The solution of this equation yields a first approximation of the electrical resistance of each part. Then, making use of the dependence of $R_i(h_i)$ obtained by the FEM model, they can be converted in thickness (h_i) values. The thin-film electrical conductivities were obtained from literature,[52,53] whereas thermal conductivities of metals

were estimated using Wiedemann–Franz law. In these assumptions, a constant ratio between bulk and thin-film conductivities is expected both for electrical and thermal terms as both magnitudes are directly proportional in metals:

$$\kappa_{film} = \kappa_{bulk} \frac{\sigma_{film}}{\sigma_{bulk}}. \tag{S3}$$

Finally, the FEM is fine-tuned by varying the thermal conductivity of the nitride thin film – which is known to significantly vary with the deposition process from 0.5 up to 8 $\mathrm{W/m{\cdot}K}$[54] – and by minor changes in the metal thin films thicknesses in order to precisely match both self-heating and furnace curve simultaneously (Figure S5). Once calibrated, a sample conductance is added to the apex of the probe in the FEM. As Figure S6 illustrates, this boundary condition allows to estimate the effects for high contact conductances on the temperature distribution of the probe. Ultimately, the variation in tip temperature caused by the presence of a highly conductive sample marks the upper limit of conductance measurable under the assumption of constant tip temperature operation.[55]

Mechanical uncertainty analysis

Systematic errors in the force curve are derived from the calibration process. They can be condensed in the coefficient $\partial F/\partial V$ used to convert the interferometer voltage readout into the force applied. It basically depends on two sources, the one associated with the tip elastic constant $K_{probe} = \partial F/\partial z$ determination and the error derived from the fit of $\partial V/\partial z$:

$$\epsilon_{\partial F/\partial V} = \sqrt{\left(\epsilon_{K_{probe}}\right)^2 + \left(\epsilon_{\partial V/\partial z}\right)^2} \tag{S4}$$

An overall systematic error is estimated in 5.6% for the force measurement. However, the stochastic variation of the measurement, i.e. the reproducibility of the steps carried out over the same point, also contributes to the uncertainty of the measurement. In those cases, an average standard variation of the global elastic constant K_{eq} is estimated to be 16.1%. Hence, the error in the estimation of the NW elastic constant is derived from the systematic error of $\partial F/\partial V$ and the average variation of K_{eq}, resulting in a total error of 17.0%.

$$\epsilon_{K_{NW}} = \sqrt{\left(\epsilon_{\partial F/\partial V}\right)^2 + \left(\sigma_{K_{eq}}\right)^2} \tag{S5}$$

Thermal uncertainty analysis

A noticeable variation was found in the electrical resistance with null dissipated power $R_{P=0}$ during the experiment. Figure S5b compares the curves taken before and after the experiment. This is likely due to drift in the electrical contact of the tip during the experiment, as the overall dependence with the dissipated power does not change. Thus, these changes are attributed to the power-independent contribution of the tip resistance and do not affect the tip calibration sensitivity α_{tip}. The effect on the calculated conductance is corrected over the experimental data by computing the dissipated heat of each curve with the resistance measured at that precise moment. Since all conductance curves are offset with their absolute value, changes in their base value produced by the tip-sample interactions can be compared safely between each data-set.

Systematic errors of the measurements can be condensed in the coefficient α_{tip} related to the slope of the inset of Figure 2 though $\alpha_{tip} = R_{tip}^{-1}\partial R/\partial T_{tip}$. This parameter is used to translate the measured electrical changes in the tip electrical resistance into changes of the thermal conductance. It can be described as:

$$\epsilon_G = \epsilon_{\alpha_{tip}} = \sqrt{\left(\epsilon_{\partial R_{tip}/\partial P}\right)^2 + \left(\epsilon_{\partial R_{tip}/\partial T}\right)^2 + \left(\epsilon_{\alpha_{Au}R_{Au}}\right)^2 + \left(\epsilon_{R_{NiCr}}\right)^2} \tag{S6}$$

where ϵ_i denotes the relative error of the variable i. The first two error terms are related to the fittings of the calibration data used ($\partial R_{tip}/\partial P$ and $\partial R_{tip}/\partial T$). Typically the uncertainty in R_{NiCr} arises from the variability of the fabrication process compared to the tip specifications. However, the values used in this work were experimentally measured and therefore the error is negligible. Then, the error of the $\alpha_{Au}R_{Au}$ product arises from the differences between reported values and the tuned values used to adjust the model to the calibration data. A high interdependence between this value and the thicknesses of the Pd and Au films was found, making this factor one of the main sources of error for the estimation of α_{tip}. Hence, the overall systematic error is estimated in 10.7%

Additionally, a source of error arises from the approximation of a constant temperature rise at the tip apex θ_{tip} during the contact event. The approximation assumes that the newly created heat pathway at the apex of the tip G_c is negligible compared to the cantilever conductance. Figure S6 illustrates the variation of θ_{tip} obtained from the FEM presented in Figure 2 upon an increasing contact conductance. For the range of G_c studied in this work, a fluctuation of 1.6% is expected.

Another source of error is related to the stochastic variation of the measurement, i.e. the reproducibility of the steps carried out over the same point. This uncertainty strongly depends on the exact point of contact and thus the contact area. An average standard variation of ΔG of 2.7% has been estimated for the case of steps over the bulk, and of 2.8% for the steps over the NWs. This results in an overall uncertainty of 3.9%. Figure 2 differentiates this error from the systematic ones described for α_{tip}.

Finally, the error in the estimation of the thermal conductivity is derived from the measurement of the actual NW diameter ϕ (5.3%), the systematic error derived from α_{tip} (3.9%), and the average variation of ΔG both on the NW and on the bulk (used to calculate the contact resistance). Hence the estimation in the thermal conductivity results in a total error of 12.5%.

$$\epsilon_{\kappa_{NW}} = \sqrt{(2\epsilon_\phi)^2 \left(\epsilon_{\alpha_{tip}}\right)^2 + (\epsilon_\theta)^2 + \left(\sigma_{\Delta G}^{NW}\right)^2 + \left(\sigma_{\Delta G}^{Bulk}\right)^2} \tag{S7}$$

Supplementary figures

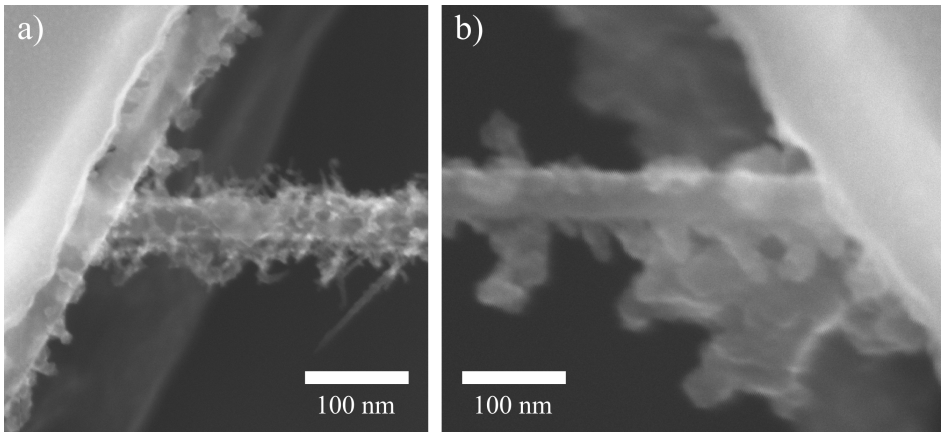

Figure S1: SEM images of the NW diameter at both ends. The geometric-mean diameter ($\phi = \sqrt{\phi_1 \phi_2}$) was used.

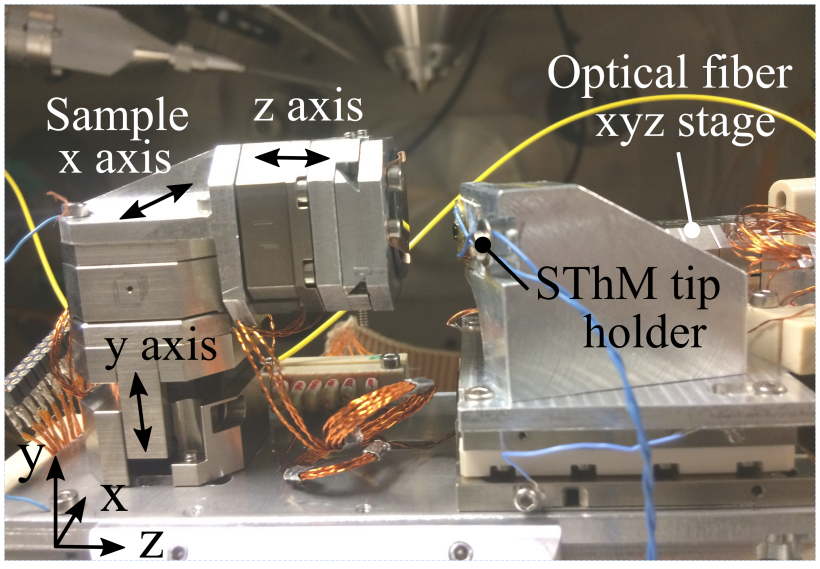

Figure S2: Image of the device inserted in the SEM chamber.

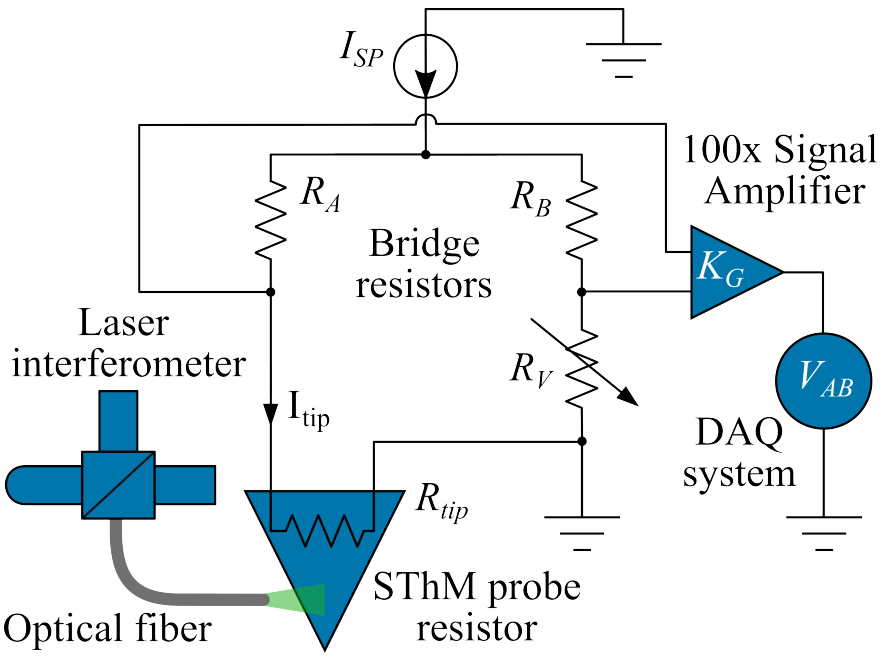

Figure S3: Diagram of the electrical and optical connection of the setup, showing the Wheatstone bridge and the interferometer used to determine tip conductance and the cantilever deflection respectively. A signal amplifier with a gain factor K_G was before reading the values with the data acquisition system (DAQ).

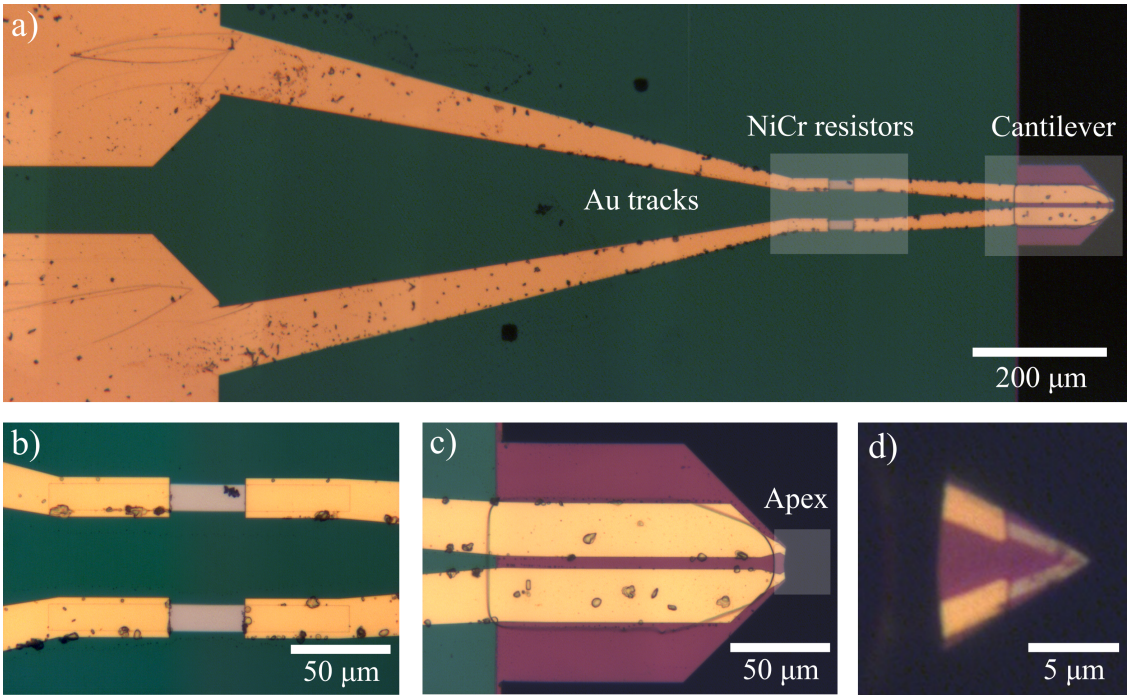

Figure S4: Optical images of the used 2nd generation Pd/nitride thin film SThM probe manufactured by KNT at different magnifications. a) Overview showing the Au tracks from the pads (left) to the cantilever. b) NiCr thin film resistance located on the bulk. c) Cantilever. d) Tip apex including the Pd resistor (grey). The image was taken tilting the tip by 45 °.

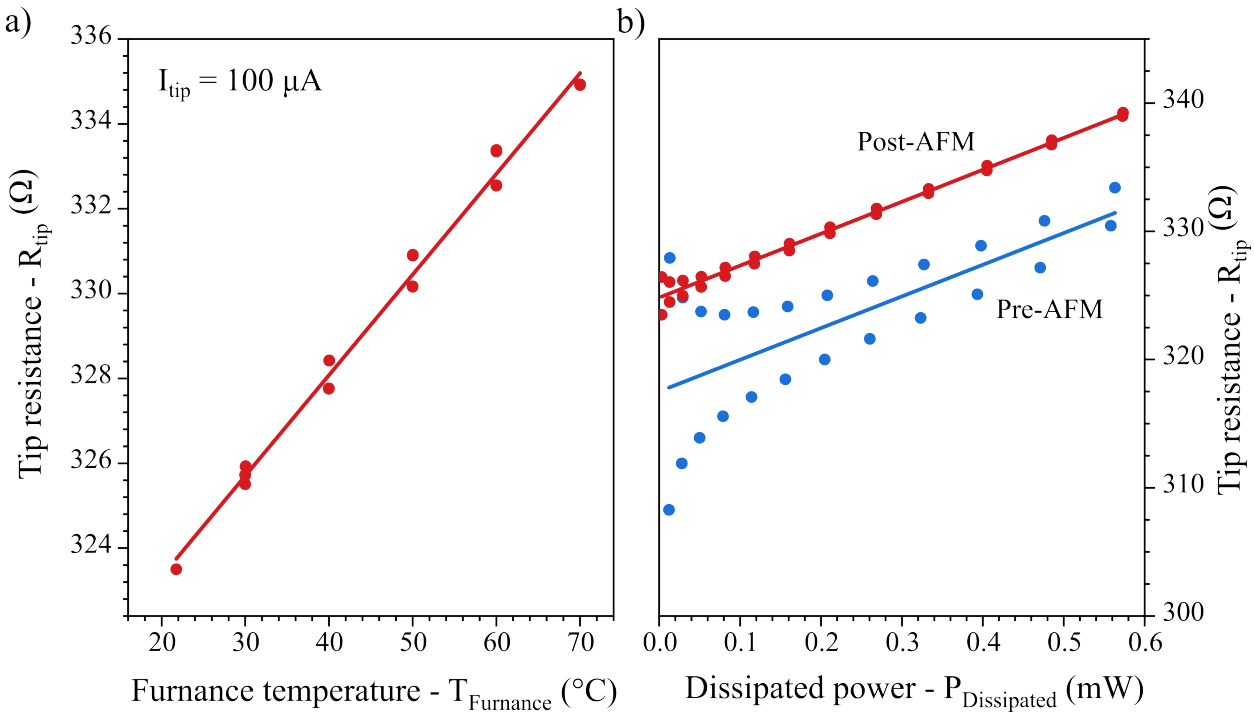

Figure S5: a) Tip resistance as a function of temperature. The value was measured using low current (100 µA) to prevent self-heating effects. b) Tip resistance as a function of the dissipated power applied to the tip. The curve was measured before and after the SThM measurements.

Table S1: Summary of the FEM parameters used to simulate the Pd/nitride thin film probe.

	Palladium		Gold		Nickel-Chromide		Nitride	
Parameter	Value	Source	Value	Source	Value	Source	Value	Source
σ (S/cm)	1.25×10^5	Ref. 52	3.1×10^4	Ref. 16	10^5	Ref. 53	-	-
α ($10^{-3}\,\mathrm{K}^{-1}$)	1.20	Ref. 16,51	2.00	Ref. 20,51	0.24	Ref. 20,51	-	-
κ (W/m·K)	23.2	Eq. S3	89.7	Eq. S3	-	-	4.3	FEM Fit
t (nm)	50	Ref. 56	140	Ref. 56	-	-	450	SEM
R_0 (Ω)	92.2	Eq. S1 and S2	45.0	Eq. S1 and S2	185.9	Exp.*	-	-

All values given at 300 K.

* Experimentally measured with microprobes.

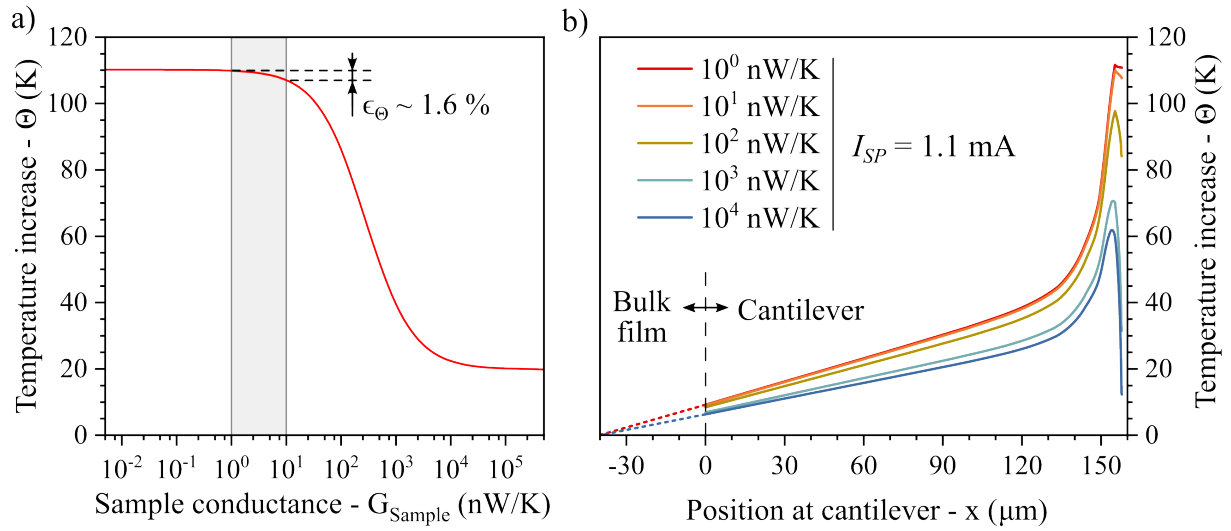

Figure S6: a) SThM probe temperature increase at the apex θ as a function of the contact conductance G_C i.e. the total sample conductance including the contact resistance when heated with a constant current of 1.1 mA (the same used during the experiments). The range of values measured in this work are highlighted with the shaded area ($1 - 10$ nW/K). b) Cantilever temperature profiles analogous to Figure 2 for contact conductances ranging from 1 nW/K to 10 μW/K.

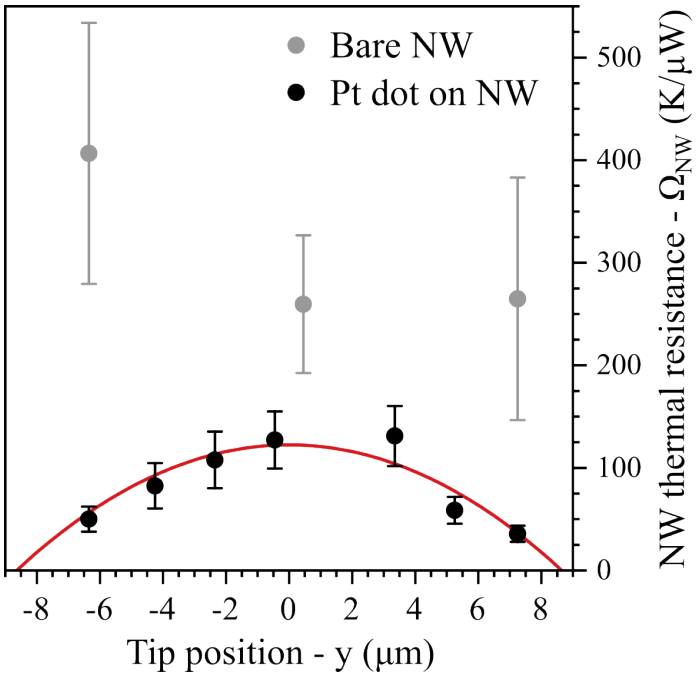

Figure S7: Nanowire local thermal resistance as a function of the tip position along the NW over Pt nanodots (black) or over bare rough surface of the NW (grey). Each point is the average of all the approach curves performed over the same point.

TOC Graphic

A combined scanning thermal microscope/scanning electron microscope (SThM/SEM) is used to characterize an expitaxially suspended silicon nanowire. Mechanical and thermal properties are measured simultaneously. Effects of the rough shell on heat dissipation and on the nanowire stiffness are studied.